

THE ACCRETION ORIGIN OF THE MILKY WAY'S STELLAR HALO

ERIC F. BELL¹, DANIEL B. ZUCKER², VASILY BELOKUROV², SANJIB SHARMA³, KATHRYN V. JOHNSTON³,
JAMES S. BULLOCK⁴, DAVID W. HOGG⁵, KNUD JAHNKE¹, JELTE T. A. DE JONG¹, TIMOTHY C. BEERS⁶, N.
W. EVANS², EVA K. GREBEL^{7,8}, ŽELJKO IVEZIĆ⁹, SERGEY E. KOPOSOV¹, HANS-WALTER RIX¹, DONALD
P. SCHNEIDER¹⁰, MATTHIAS STEINMETZ¹¹, AND ADI ZOLOTOV⁵

¹ Max-Planck-Institut für Astronomie, Königstuhl 17, D-69117 Heidelberg, Germany; bell@mpia.de

² Institute of Astronomy, University of Cambridge, Madingley Road, Cambridge CB3 0HA, UK

³ Department of Astronomy, Columbia University, 550 West 120th Street, New York, NY 10027, USA

⁴ Center for Cosmology, Department of Physics and Astronomy, University of California, Irvine, CA 92697, USA

⁵ Center for Cosmology and Particle Physics, Department of Physics, New York University, 4 Washington Place #424, New York, NY 10003, USA

⁶ Department of Physics and Astronomy, Center for the Study of Cosmic Evolution and Joint Institute for Nuclear Astrophysics, Michigan State University, E. Lansing, MI 48824, USA

⁷ Astronomical Institute, Department of Physics & Astronomy, University of Basel, Venusstrasse 7, CH-4102 Binningen, Switzerland

⁸ Astronomisches Rechen-Institut, Zentrum für Astronomie, Universität Heidelberg, Mönchhofstr. 12–14, D-69120 Heidelberg, Germany

⁹ University of Washington, Dept. of Astronomy, Box 351580, Seattle, WA 98195, USA

¹⁰ Department of Astronomy and Astrophysics, The Pennsylvania State University, University Park, PA, USA

¹¹ Astrophysical Institute Potsdam, An der Sternwarte 16, D-14482 Potsdam, Germany

THE ASTROPHYSICAL JOURNAL: *to appear June 20, 2008*

ABSTRACT

We have used data from the Sloan Digital Sky Survey (SDSS) Data Release 5 to explore the overall structure and substructure of the stellar halo of the Milky Way using ~ 4 million color-selected main sequence turn-off stars with $0.2 < g - r < 0.4$ and $18.5 \leq r < 22.5$. We fit oblate and triaxial broken power-law models to the data, and found a ‘best-fit’ oblateness of the stellar halo $0.5 < c/a < 0.8$, and halo stellar masses between Galactocentric radii of 1 and 40 kpc of $3.7 \pm 1.2 \times 10^8 M_{\odot}$. The density profile of the stellar halo is approximately $\rho \propto r^{-\alpha}$, where $-2 > \alpha > -4$. Yet, we found that all smooth and symmetric models were very poor fits to the distribution of stellar halo stars because the data exhibit a great deal of spatial substructure. We quantified deviations from a smooth oblate/triaxial model using the RMS of the data around the model profile on scales $\gtrsim 100$ pc, after accounting for the (known) contribution of Poisson uncertainties. Within the DR5 area of the SDSS, the fractional RMS deviation σ /total of the actual stellar distribution from any smooth, parameterized halo model is $\gtrsim 40\%$: hence, the stellar halo is highly structured. We compared the observations with simulations of galactic stellar halos formed entirely from the accretion of satellites in a cosmological context by analyzing the simulations in the same way as the SDSS data. While the masses, overall profiles, and degree of substructure in the simulated stellar halos show considerable scatter, the properties and degree of substructure in the Milky Way’s halo match well the properties of a ‘typical’ stellar halo built exclusively out of the debris from disrupted satellite galaxies. Our results therefore point towards a picture in which an important fraction of the stellar halo of the Milky Way has been accreted from satellite galaxies.

Subject headings: Galaxy: halo — Galaxy: formation — Galaxy: evolution — galaxies: halo — Galaxy: structure — Galaxy: general

1. INTRODUCTION

The stellar halo of the Milky Way has a number of distinctive characteristics which make it a key probe of galaxy formation processes. Milky Way halo stars have low metallicity, alpha element enhancement, a high degree of support from random motions, and a roughly r^{-3} power law distribution in an oblate halo (Eggen, Lynden-Bell & Sandage 1962; Chiba & Beers 2000; Yanny et al. 2000; Larsen & Humphreys 2003; Lemon et al. 2004; Newberg & Yanny 2005; Jurić et al. 2007). The low metallicities and alpha element enhancements suggest that the stars formed relatively early in the history of the Universe. Yet, there has been disagreement about where these stars formed: did they form *in situ* in the early phases of the collapse of the Milky Way (e.g., Eggen, Lynden-Bell & Sandage 1962), or did the stars form outside the Milky Way in satellite galaxies only to be accreted by the Milky Way at a later date (e.g., Searle & Zinn 1978; Majewski, Munn, & Hawley 1996; Bullock, Kratsov, & Weinberg 2001; Bullock & Johnston 2005; Abadi, Navarro, & Steinmetz 2006)?

A key discriminant between these pictures is the structure of the stellar halo (Majewski 1993). *In situ* formation would predict relatively little substructure, as the formation epoch was many dynamical times ago. In contrast, current models of galaxy formation in a hierarchical context predict that the vast majority of stellar halo stars should be accreted from disrupted satellite galaxies (Johnston 1998; Bullock, Kratsov, & Weinberg 2001; Bullock & Johnston 2005; Moore et al. 2006; Abadi, Navarro, & Steinmetz 2006). The accumulated debris from ancient accretion episodes rapidly disperses in real space (although in phase space, some information about initial conditions persists; e.g., Helmi & White 1999), forming a relatively smooth stellar halo. The debris from accretions in the last few Gyr can remain in relatively distinct structures. Simulations predict quite a wide range in ‘lumpiness’ of stellar halos, with a general expectation of a significant amount of recognizable halo substructure (Bullock, Kratsov, & Weinberg 2001; Bullock & Johnston 2005).

Consequently, a number of groups have searched for sub-

structure in the Milky Way’s stellar halo, identifying at least 3 large-scale features — tidal tails from the disruption of the Sagittarius dwarf galaxy, the Low-Latitude stream, and the Virgo overdensity (Ibata, Gilmore, & Irwin 1995; Yanny et al. 2000; Ivezić et al. 2000; Newberg et al. 2002; Majewski et al. 2003; Yanny et al. 2003; Ibata et al. 2003; Jurić et al. 2007; Duffau et al. 2006; Belokurov et al. 2006a; Newberg et al. 2007, although see Momany et al. 2006 for a discussion of possible disrupted disk origin of much of the Low-Latitude stream) — and a host of tidal tails from globular clusters (e.g., Odenkirchen et al. 2003; Grillmair & Johnson 2006), dwarf galaxies (e.g., Irwin & Hatzidimitriou 1995; Martínez-Delgado et al. 2001), and of unknown origin (e.g., Belokurov et al. 2006b; Grillmair 2006a; Grillmair & Dionatos 2006; Belokurov et al. 2007). Furthermore, substructure has been observed in the stellar halos of other galaxies (e.g., Shang et al. 1998; Ibata et al. 2001). Thus, it is clear that accretion of stars from satellite galaxies is a contributor to the stellar halos of galaxies.

Yet, it remains unclear whether accretion is the *dominant* mechanism for halo build-up. A key observable is the fraction of stars in substructure (or a quantitative measure of the degree of substructure): if much of the halo mass is held in substructures, this argues for an accretion origin; if instead a tiny fraction of halo stars is held in substructures, this places (very) tight constraints on any recent accretion scenario. However, it is not clear how best to address this question. One possible approach is to define ‘overdense’ areas of the halo by hand or algorithmic means, and to fit the rest with a smooth halo component; the remainder would be in ‘overdensities’ (e.g., Newberg & Yanny 2005). Here, we take a different approach. Since one does not know *a priori* which stars should be ‘smooth halo’ stars and which are in ‘overdensities’, we treat all halo stars equally, fit a smooth model, and examine the RMS of the data around that smooth model (accounting for the contribution to the RMS from counting statistics). In this way, we obtain a quantitative measure of the degree of halo structure on $\gtrsim 100$ pc scales without having to make uncomfortable decisions about which stars should be fit with a smooth component and which should be included in overdensities.

In this paper, we apply this technique to explore the structure of the stellar halo of the Milky Way, and place constraints on the fraction of stars in stellar halo under- or over-densities using imaging data from the Fifth Data Release (DR5) of the Sloan Digital Sky Survey (SDSS; York et al. 2000; Adelman-McCarthy et al. 2007). Under the assumption that the bulk of the stellar population in the stellar halo is relatively metal-poor and old, we isolate a sample dominated by halo main sequence turn-off stars and explore the distribution of halo stars as a function of Galactic latitude, longitude and distance from the Sun (§2). In §3, we generate a grid of smooth halo models to compare with the data, and in §4 we constrain the ‘best-fit’ smooth stellar halo parameters and quantify the fraction of halo stars in stellar halo under- or over-densities. We compare the observations with models of stellar halo formation in a cosmological context in §5, and present a summary in §6.

2. DATA

SDSS is an imaging and spectroscopic survey that has mapped $\sim 1/4$ of the sky. Imaging data are produced simultaneously in five photometric bands, namely u , g , r , i , and z (Fukugita et al. 1996; Gunn et al. 1998; Hogg et al. 2001; Gunn et al. 2006). The data are processed through pipelines to measure photometric and astrometric properties (Lupton, Gunn, & Szalay 1999;

Stoughton et al. 2002; Smith et al. 2002; Pier et al. 2003; Ivezić et al. 2004; Tucker et al. 2006) and to select targets for spectroscopic follow-up. DR5 covers ~ 8000 square degrees around the Galactic North Pole, together with 3 strips in the Galactic southern hemisphere. We use the catalog of objects classified as stars with artifacts removed¹, together with magnitude limits $r < 23.5$ and $g < 24.5$. Photometric uncertainties as a function of magnitude are discussed in Sesar et al. (2007). We choose to analyze only the largely contiguous ~ 8000 square degree area around the Galactic North Pole in this work, giving a total sample of $\sim 5 \times 10^7$ stars, of which $\sim 3.6 \times 10^6$ stars meet the selection criteria we apply later. In what follows, we use Galactic extinction corrected magnitudes and colors, following Schlegel et al. (1998); such a correction is appropriate for the stars of interest in this paper owing to their large heliocentric distances $D_{\text{heliocentric}} \gtrsim 8$ kpc.

2.1. Color–magnitude diagrams: an introduction

To help get one’s bearings, it is instructive to examine some color–magnitude diagrams (CMD) derived from these data (Fig. 1). The color–magnitude diagram of all stars with $b > 30^\circ$ is shown in the top left panel, where the grey levels show the logarithm of the number of stars in that bin per square degree from 10^{-3} stars/deg² to 7.1 stars/deg²; such a scaled CMD is frequently called a Hess diagram. To help interpret this Hess diagram, we show two additional Hess diagrams for two globular clusters covered by these data: Pal 5 and NGC 5024 (in what follows, distances and metallicities for these and all other globular clusters are adopted from Harris 1996). The top middle panel of Fig. 1 shows a Hess diagram for stars in the globular cluster Pal 5 (a circle of radius 0.5° around the position $l = 0.0^\circ 85$ and $b = 45.9^\circ$). The grey levels show:

$$(N_{\text{on}}A_{\text{on}}^{-1} - N_{\text{off}}A_{\text{off}}^{-1})/N_{\text{off}}A_{\text{off}}^{-1}, \quad (1)$$

where N denotes the number of stars in the field of interest (denoted by the subscript ‘on’) and a control field ‘off’, and A is the area of that field. In this case the control field is nearby: a circle of radius 4° around the position $l = 6^\circ$ and $b = 46^\circ$. One can clearly see the main sequence turn off with $g-r \sim 0.2$ and $r \sim 21$, with the lower main sequence extending redwards towards fainter magnitudes and the subgiant branch extending redwards towards brighter magnitudes. In the top right panel we show a similar Hess diagram for NGC 5024; because this cluster is rather brighter than Palomar 5 the CMD is better populated and shows a more prominent red giant branch (extending towards brighter magnitudes with $g-r \sim 0.5$) and horizontal branch (with $g-r \lesssim 0$ and $r \sim 17$).

There are a few points to note about Fig. 1. Firstly, for old populations such as those in globular clusters it is clear that the color of the main sequence turn-off (MSTO) is a metallicity indicator (this point is discussed in more detail for SDSS isochrones in Girardi et al. 2004). Comparing Pal 5 ($[\text{Fe}/\text{H}] \sim -1.4$, $(g-r)_{\text{MSTO}} \sim 0.3$) with NGC 5024 ($[\text{Fe}/\text{H}] \sim -2.1$, $(g-r)_{\text{MSTO}} \sim 0.15$), one can see that old very metal-poor populations ($[\text{Fe}/\text{H}] \lesssim -2$) have bluer main sequence turn-offs compared to less metal-poor populations ($[\text{Fe}/\text{H}] \sim -1.5$). Second, MSTO stars are a reasonably good distance indicator, albeit with significant scatter. In Fig. 2, we show the absolute magnitude distribution of all stars with $0.2 < g-r < 0.4$ in Pal 5 (solid line: distance= 22.6 kpc), NGC 5024 (dashed line: distance= 18.4 kpc) and a third globular cluster NGC 5053 (dotted line: $[\text{Fe}/\text{H}] \sim -2.3$, distance= 16.2 kpc). The mean r -band

¹See <http://cas.sdss.org/astro/en/help/docs/realquery.asp#fl>

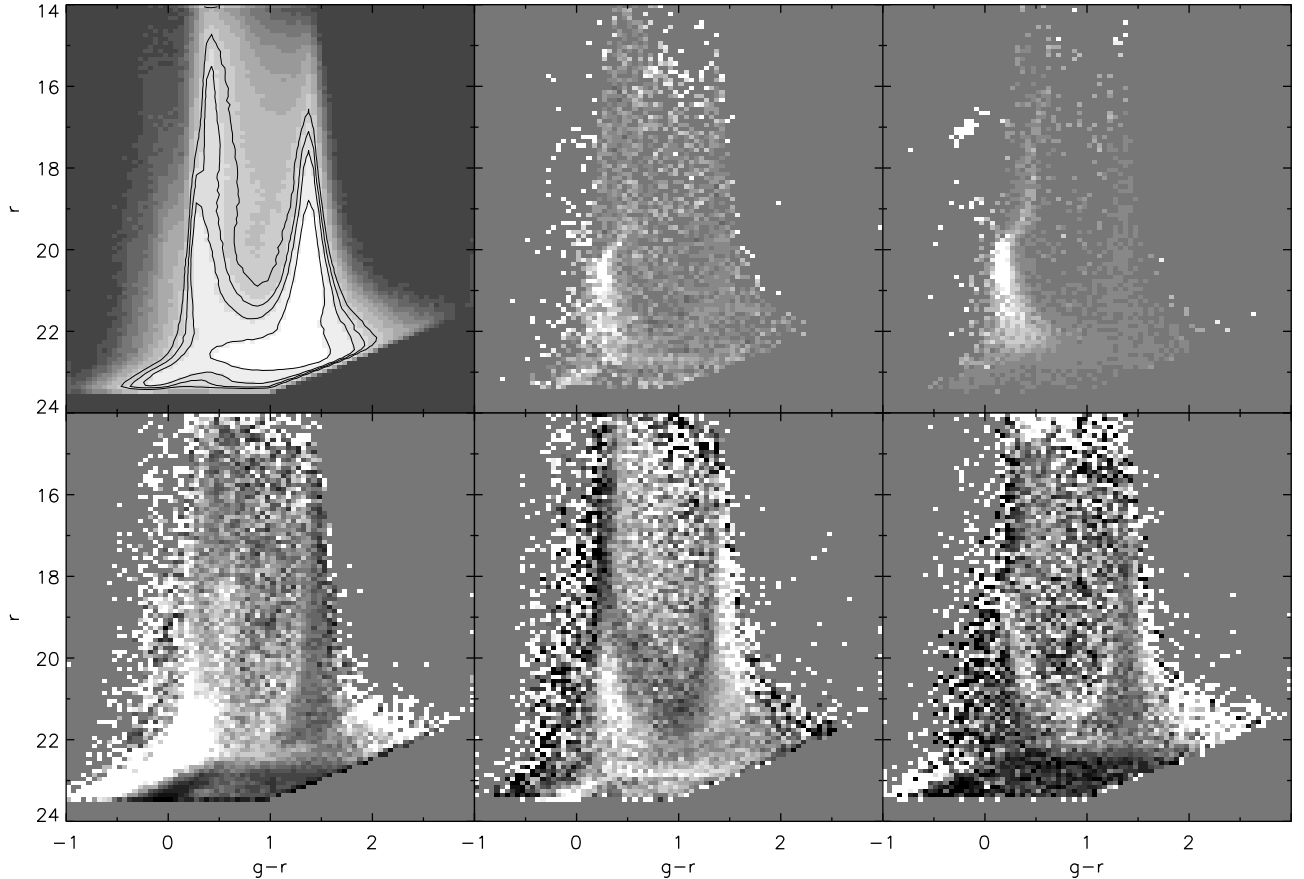


FIG. 1.— Hess diagrams in terms of $g-r$ color and r -band magnitude derived from the SDSS data. In these Hess diagrams, we show for completeness the data to the very faintest limits $r \gtrsim 23$, where the S/N is low and there is significant contamination by misclassified galaxies, spurious detections, etc. These diagrams show in general two plumes in the stellar density distribution that reflect main sequence turn-off stars with $g-r \sim 0.3$ and intrinsically faint and low-mass disk dwarf stars with $g-r \sim 1.4$. We limit our analysis to $18.5 \leq r < 22.5$ in this paper for the main sequence turn-off dominated color bin $0.2 < g-r < 0.4$, in the area where the data quality is still excellent. **Top left:** The density of stars per square degree per color interval per magnitude for $b > 30^\circ$, scaled logarithmically. This Hess diagram contains 4×10^7 stars. **Top middle:** The Hess diagram for the (sparsely-populated) globular cluster Pal 5 (within a circle of radius 0.5°). **Top right:** The Hess diagram for the globular cluster NGC 5024. **Bottom left:** A difference Hess diagram (following Eqn. 1) differencing two lines of sight $(l, b) = (300, 70)$ and $(l, b) = (60, 70)$. The grey scales saturate at $\pm 100\%$. In an axisymmetric halo, this difference should equal zero within the shot noise: it clearly does not. **Bottom middle:** A difference Hess diagram differencing two lines of sight $(l, b) = (44, 40)$ and $(l, b) = (15, 45)$. The grey scales saturate at $\pm 50\%$. This Hess diagram should be close to, but not exactly equal to, zero. **Bottom right:** A difference Hess diagram differencing two lines of sight $(l, b) = (167, 35)$ and $(l, b) = (193, 35)$. The grey scales saturate at $\pm 50\%$. Again, in a symmetric halo, this difference should equal zero.

absolute magnitudes of the distributions are (4.3,4.7,5.0) respectively, and all distributions individually have $RMS \sim 0.9$ mag. Thus, modulo a metallicity-dependent $\lesssim 0.5$ systematic uncertainty, the MSTO is a good distance indicator with ~ 0.9 mag scatter.

Examining the top left panel of Fig. 1, in the light of the globular cluster CMDs, it is possible to interpret some of the features of the $b > 30^\circ$ Hess diagram. At all distances, the MSTO is visible as a clearly-defined as a sharp ‘blue edge’ to the distribution, indicating to first order that the stars in the galactic disk at large scale heights and in the stellar halo are dominated by a metal-poor old population with ages not that dissimilar to those of globular clusters; this is the assumption that we will adopt in the remainder of this paper. At $g-r < 0.5$, one sees the MSTO for stars in the stellar disk at $\gtrsim \text{kpc}$ scale heights (at $r < 18$; often the disk at such scale heights is referred to as the thick disk) and in the stellar halo (at $r > 18$). One can see a ‘kink’ in the MSTO at $r \sim 18$, as highlighted by the contours; we interpret this as signifying a metallicity difference between the disk at $\sim \text{kpc}$ scale heights and stellar halo (this transition

is also very prominent in Fig. 4 of Lemon et al. 2004 and in Chen et al. 2001, who interpret this CMD feature in the same way). The MSTO in the stellar halo has $g-r \sim 0.3$, similar to that of Pal 5 ($[\text{Fe}/\text{H}] \sim -1.4$) and ~ 0.15 mag redder than those of NGC 5024 and NGC 5053 with ($[\text{Fe}/\text{H}] \lesssim -2$). This suggests a halo metallicity $[\text{Fe}/\text{H}] \sim -1.5$, in excellent agreement with measured halo metallicity distributions, which peak at $[\text{Fe}/\text{H}] \sim -1.6$ (e.g., Laird et al. 1998; Venn et al. 2004).

2.2. Hess diagrams of structure in the stellar halo

One of the main goals of this paper is to explore the degree of substructure in the stellar halo of the Milky Way. One way of visualizing this issue is through the inspection of Hess diagrams where pairs of lines of sight are subtracted, following Eqn. 1². We have done this exercise for three such lines of sight in Fig. 1, where we have chosen three line-of-sight pairs where the

²An extension of this methodology was used by Xu et al. (2006), who use the SDSS DR4 to study stellar halo structure using star counts and color distributions of stars at Galactic latitudes $b \geq 5^\circ$.

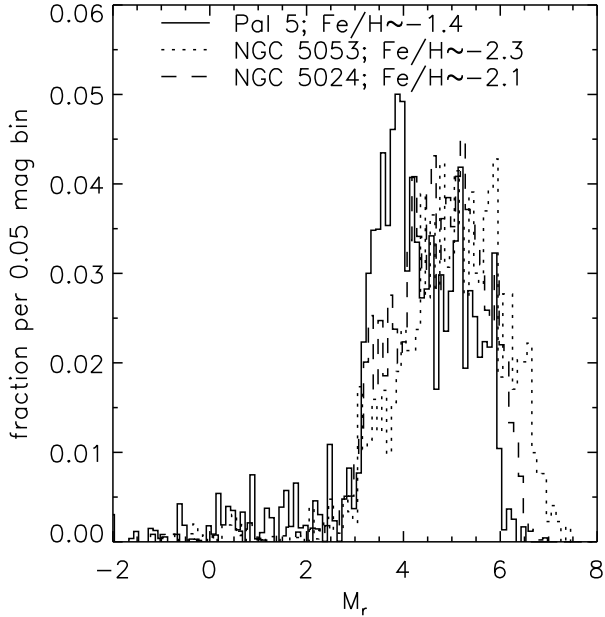


FIG. 2. — A histogram of the absolute magnitudes of stars with $0.2 < g-r < 0.4$ in three globular clusters: Pal 5, NGC 5053, and NGC 5024. These distributions give an impression of the actual convolution kernel suffered by the $0.2 < g-r < 0.4$ MSTO stars in the halo of the Milky Way when going from distance to apparent magnitude. In this work, we choose to approximate this distribution for modeling the stellar halo with a Gaussian distribution with $\langle M_r \rangle = 4.5$ mag and $\sigma_{M_r} = 0.9$ mag, an appropriate choice for a stellar population with $[\text{Fe}/\text{H}] \sim -1.5$.

subtraction *should* have been close to zero, if the stellar halo of the Milky Way were symmetric and smooth.

The lower left panel of Fig. 1 shows the difference of two different lines of sight $(l, b) = (300, 70)$ — a line of sight towards the Virgo overdensity and a part of the Sagittarius stream — and $(l, b) = (60, 70)$; in a symmetric model such a subtraction should come out to zero. The grey levels saturate at deviations of $\pm 100\%$. It is clear that the $(l, b) = (300, 70)$ line-of sight has strong order-of-unity overdensities at MSTOs fainter than $r > 21$, or distances of > 20 kpc assuming a MSTO absolute magnitude of $M_r \sim 4.5$. One can see also a weak sub-giant and red giant branch feature at $g-r \sim 0.5$ and $18 < r < 20$, again indicating distances > 20 kpc.

The lower middle shows a line of sight towards $(l, b) = (44, 37)$ minus the Hess diagram for stars towards $(l, b) = (15, 41)$. This subtraction would be expected to come out close to, but not exactly, zero. It would be ideal to be able to subtract off the ‘correct’ pairing of $(l, b) = (316, 37)$; however, SDSS has not mapped that area of sky owing to its southern declination, $\delta = -25$. The grey scale saturates at $\pm 50\%$. There are minor artifacts in the subtraction; however, one can clearly see an overdensity of main sequence stars with a MSTO with $r \sim 20.5$, corresponding to a distance of ~ 16 kpc.

The lower-right panel shows a line of sight towards $(l, b) = (167, 35)$ — a line of sight towards part of the Low-Latitude overdensity — minus that of $(l, b) = (193, 35)$. In a symmetric halo this subtraction should be identically zero. The grey scale saturates at $\pm 50\%$. There is a weak MSTO overdensity at $r \sim 19$ mag, some ~ 7 kpc from the observer.

While these lines of sight have been selected to show (vary-

ing degrees) of halo inhomogeneity³, they suffice to illustrate two key points. First, the halo is far from homogeneous, with strong order-of-unity overdensities as well as weaker ~ 10 – 20% features. Second, owing to the partial sky coverage of the SDSS, it is difficult to visualize and quantitatively explore the structure of the Milky Way’s stellar halo using CMD subtractions.

2.3. Main sequence turn-off star maps of the stellar halo

One more intuitive approach to the distribution of stars in the stellar halo is to construct maps of the number of MSTO stars in different magnitude (therefore, roughly distance) slices. We select MSTO stars with foreground extinction-corrected $0.2 < g-r < 0.4$; this color range was selected empirically to encompass the most densely-populated bins of color space for the halo MSTO stars in Fig. 1. In §2.1, we showed that in such a color bin the average absolute magnitude of the MSTO stars in that bin were 4.3 and 4.7 respectively for Palomar 5 ($[\text{Fe}/\text{H}] \sim -1.4$) and NGC 5024 ($[\text{Fe}/\text{H}] \sim -2.1$); accordingly, we adopt an average MSTO $M_r = 4.5$ in what follows for stars in the color bin $0.2 < g-r < 0.4$. Such an absolute magnitude is in agreement with model CMDs, which suggest $M_r = 4.7 \pm 0.2$ for stars with metallicities $[\text{Fe}/\text{H}] \sim -1.5 \pm 0.5$. We make the assumption that all stars in the stellar halo are ‘old’ (i.e., approximately the same age as the calibrating globular clusters).

We show 0.5 mag wide bins of r -band magnitude between $18.5 \leq r < 22.5$, corresponding to heliocentric distances of $7 \lesssim d/\text{kpc} \lesssim 40$. At such heliocentric distances, the vertical distance above the Galactic plane is $\gtrsim 5$ kpc along all lines of sight, or at $\gtrsim 5$ scale heights following the ~ 900 pc thick disk scale height estimated by Larsen & Humphreys (2003). Thus, the dominant contribution to the MSTO maps is from the stellar halo. The resulting Lambert azimuthal equal-area polar projections, logarithmically-scaled, are shown in Fig. 3⁴.

While one loses the ability to probe for population differences in the stellar halo because of the broad color bin adopted to derive these densities, it is much more straightforward to visualize the distribution of halo MSTO stars using this technique. From Figs. 1 and 2, one can see that MSTO stars at a single distance will show up in multiple distance bins: the bins are 0.5 mag wide, and the RMS of a single distance stellar population is ~ 0.9 mag. This can be seen easily from inspection of some of the ‘hot pixels’ in Fig. 3, corresponding to known globular clusters or dwarf galaxies. These features persist from map-to-map despite there being a single population at a unique distance, giving a visual impression of the covariance between the different maps.

³Although, in fact, we found it impossible to avoid at least low-level inhomogeneity along any pair of lines of sight.

⁴This presentation is similar to that of Fig. 24 of Jurić et al. (2007), who present this kind of analysis for $20 < r < 21$, and Newberg et al. (2007), who present a similar diagram with slightly more restrictive color cuts for $20 < g < 21$.

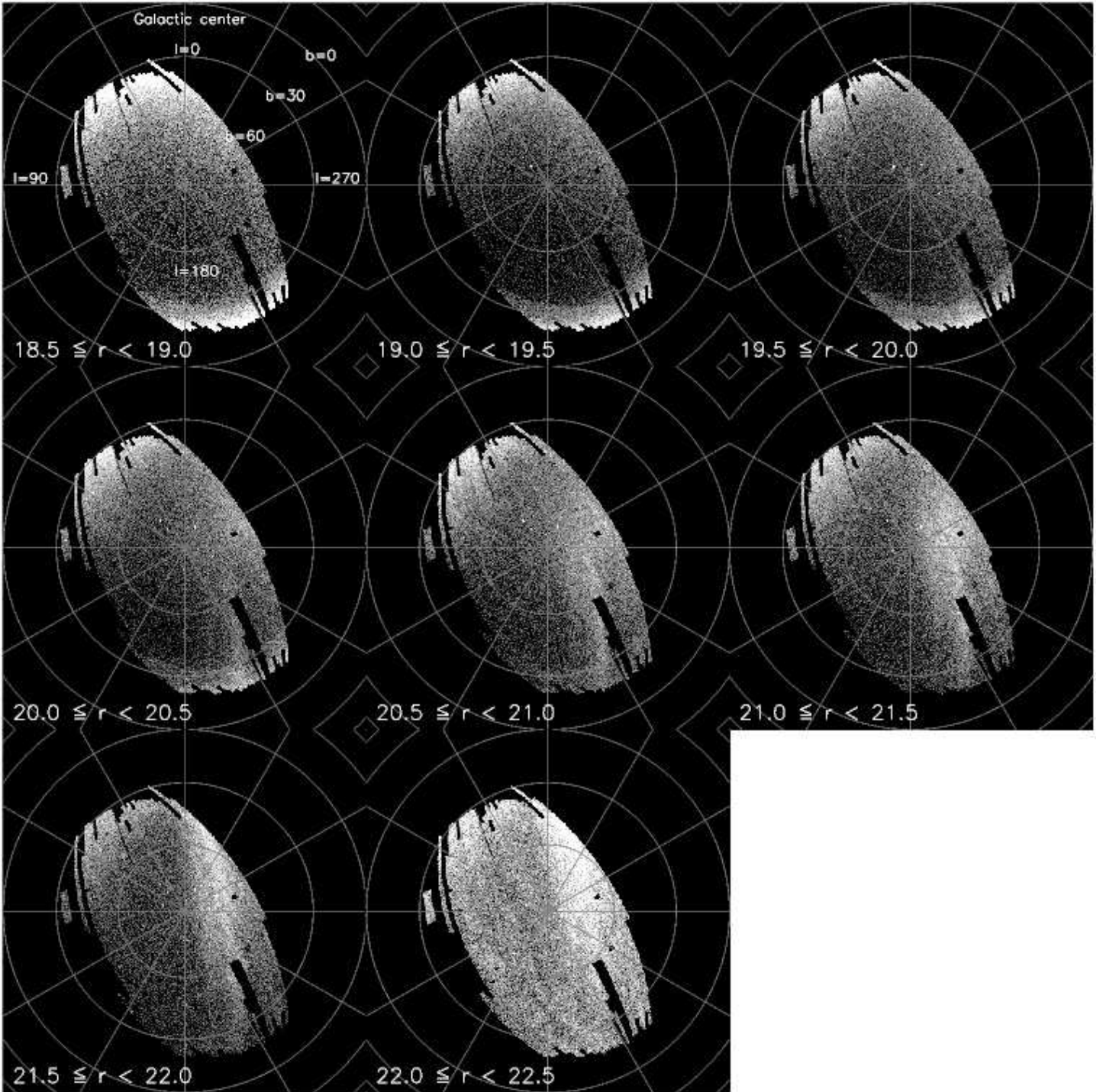


FIG. 3.— The stellar halo of the Milky Way as seen by SDSS. The grey scale denotes the logarithm of the number density of $0.2 \leq g-r \leq 0.4$ stars per square degree in eight different magnitude (therefore mean distance) slices; a Lambert azimuthal equal-area polar projection is used. The black areas are not covered by the SDSS DR5, and reflect the great circle scanning adopted by the SDSS when collecting its imaging data. Apparent ‘hot pixels’ are stellar overdensities from globular clusters and dwarf galaxies.

Focusing on the brightest bins, $18.5 \leq r < 20$, corresponding to heliocentric distances between ~ 7 kpc and ~ 11 kpc, the stellar distribution appears rather smooth, with higher density towards the Galactic center and Galactic anticenter. In the case of the Galactic center, the interpretation is straightforward: one is probing lines of sight which pass ~ 5 kpc from the Galactic center, and probe the denser inner parts of the stellar halo. In the case of the Galactic anticenter, such a structure is not expected in an oblate/triaxial halo model, and recalling the $\lesssim 1$ kpc scale height of the thick disk cannot be a thick disk; this is the well-known Low-Latitude stream (e.g., Newberg et al. 2002; Peñarrubia et al. 2005; Momany et al. 2006). In this visualization, the stream appears to be spread out between a few different magnitude bins: at $b < 30^\circ$ some of that spread may be real, but the well-defined structure at $(l, b) \sim (165, 35)$ has a relatively narrow distance spread (see the Hess diagram residual in the lower right-hand panel of Fig. 1, showing a reasonably narrow main sequence; see also the discussion in Grillmair 2006b).

Focusing on the more distant bins, $20 \leq r < 22.5$, corresponding to heliocentric distances between ~ 14 kpc and ~ 35 kpc, one finds little contribution from the Low-Latitude stream. Instead, superimposed on a reasonably smooth background is a prominent contribution from large tidal tails from the ongoing interaction of the Milky Way with the Sagittarius dwarf galaxy (see Belokurov et al. 2006a, for a much more detailed discussion). As quantified by Belokurov et al. (2006a), one can discern a distance gradient in the stream, from the closest populations towards the Galactic anticenter $(l, b) \sim (200, 20)$ to the most distant populations towards $(l, b) \sim (340, 50)$.

While it is clear from these maps that the stellar halo of the Milky Way is not completely smooth, there is a ‘smooth’ (i.e., not obviously structured) component which dominates these maps: if there are variations in this component, these must be on spatial scales $\gtrsim 10^\circ$ on the sky (or scales $\gtrsim 1$ kpc at the distances of interest for this paper). A number of methods could be devised to probe halo structures on such scales. In this paper, we choose to construct models of a smooth stellar halo to represent the Milky Way, and to ask about the fraction of stars deviating from this smooth global model as a measure of substructure in the halo. This exercise is the topic of the remainder of this paper.

3. MODELS OF A SMOOTHLY-DISTRIBUTED STELLAR HALO

The stellar halo of the Milky Way is modeled using an triaxial broken power-law, where we explore oblate and prolate distributions as special cases of triaxial. The minor axis of the ellipsoid is constrained to be aligned with the normal to the Galactic disk (this is in contrast with Newberg & Yanny 2005 and Xu et al. 2006, who allow the minor axis to vary freely). There are 7 free parameters: the normalization A (constrained directly through requiring that the model and observations have the same number of stars in the magnitude and color range considered in this paper), the two power laws α_{in} and α_{out} , the break radius r_{break} , b/a , c/a , and the Galactocentric longitude of the major axis L_{major} . We adopt a grid search, with between 4 and 10 values in each parameter of interest, yielding typically several hundred to several thousand smooth models to test against the data. In what follows, we assume a distance to the Galactic center of 8 kpc and a $M_r = 4.5$ for the MSTO stars with $0.2 < g-r < 0.4$, with a $\sigma_{M_r} = 0.9$ mag.

We choose to define the best fit to be the fit for which the RMS deviation of the data σ around the model is minimized, taking account of the expected Poisson counting uncertainty in

the model, summed over all bins in l , b , and magnitude:

$$\langle \sigma^2 \rangle = \frac{1}{n} \sum_i (D_i - M_i)^2 - \frac{1}{n} \sum_i (M'_i - M_i)^2 \quad (2)$$

$$\sigma/\text{total} = \frac{\sqrt{\langle \sigma^2 \rangle}}{\frac{1}{n} \sum_i D_i}, \quad (3)$$

where D_i is the observed number of main-sequence turn-off stars in bin i , M_i is the exact model expectation of that bin, M'_i is a realization of that model drawn from a Poisson distribution with mean M_i , and n is the number of pixels. We could have chosen instead to define the best fit by minimizing the reduced χ^2 :

$$\chi^2 = \sum_i (D_i - M_i)^2 / \sigma_i^2, \quad (4)$$

where σ_i^2 is the Poisson uncertainty of the model M_i ⁵. We have chosen not to do so in this case because we are interested in quantifying and placing a lower limit on the structure in the stellar halo in this paper, not in finding the ‘best’ fit to the stellar halo in a χ^2 sense (we show in §4 that the stellar halo model with the lowest χ^2 has a σ/total that is close to, but slightly higher than the stellar halo model with lowest σ/total). For the purposes of substructure quantification, σ/total has two decisive advantages. Firstly, unlike χ^2 , σ/total is *independent* of pixel scale,⁶ provided that the substructure in the halo is well-sampled by the chosen binning scale. Secondly, for σ/total , the contribution of Poisson noise to σ has been removed, leaving only the contribution of actual halo structure to the variance⁷. Thus, even though we have adopted a pixel size of $0.5^\circ \times 0.5^\circ$ in what follows (corresponding to > 100 pc scales at the distances of interest), our results are to first order independent of binning scale (because empirically we find that the vast majority of the variance is contained on \sim kpc scales and greater). We defer to a future paper the exercise of understanding and interpreting the scale dependence of stellar halo substructure. The main uncertainty in the estimated values of σ/total is from the major contributions of a few large structures on the sky to σ/total , both through influencing the ‘best fit’ and through their direct contribution to the residuals. Later, we attempt to quantify this uncertainty through exclusion of the most obvious substructures from consideration before fitting and estimation of σ/total .

The model parameters (including the normalization) give an estimate of the total number of stars in the halo. We calculate the total number of stars contained in the model with Galactocentric radius $1 \leq r_{\text{GC}}/\text{kpc} \leq 40$. In order to interpret this value as a mass, it is necessary to convert the number of $0.2 < g-r < 0.4$ stars into a mass by calculating a mass-to-number ratio. We adopt an empirical approach, following Newberg & Yanny (2005). Given that the Pal 5 MSTO color seems to be a good match to the stellar halo MSTO color, we use the mass of Pal 5 ($\sim 5000 M_\odot$; Odenkirchen et al. 2002) and the number of stars in Pal 5 above background (~ 1069 stars with $0.2 < g-r < 0.4$) to define a mass-to-number ra-

⁵The uncertainty in the model is chosen here because we are evaluating the likelihood of the dataset being drawn from the model.

⁶The quantity $\sqrt{\langle \sigma^2 \rangle}$ is inversely proportional to n in the presence of intrinsic structure in the dataset, as is the quantity $\frac{1}{n} \sum_i D_i$, thus making σ/total pixel scale independent.

⁷We have confirmed by rebinning the data by factors of 16 in area that σ/total is indeed independent of pixel scale; thus, the dominant contribution to the intrinsic structure of the stellar halo must be on linear scales $\gtrsim 400$ pc.

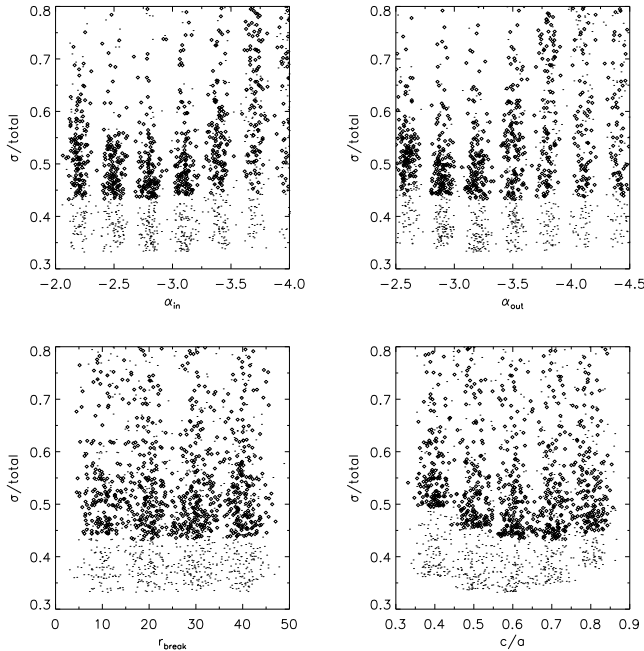


FIG. 4.— The σ/total of a large number of *oblate* halo models. Each point represents the value of σ/total for a different oblate halo model: open diamonds show the residuals when no clipping is applied, points show the result when areas with contributions Sgr/Low-Latitude stream/Virgo are excised before carrying out the analysis. In each case, we show the values of σ/total as a function of α_{in} , α_{out} , r_{break} and c/a , marginalized over all other model parameters. Recall that our definition of σ/total subtracted off the Poisson uncertainties already, and is a measure of the degree of substructure on scales $\gtrsim 100$ pc. It is clear that the oblateness c/a of the halo is the best-constrained parameter; combinations of all of the other parameters can provide equally-good fits, given an oblateness. Small random offsets are applied to the discrete values of α_{in} , α_{out} , r_{break} and c/a to aid visibility.

tio $\sim 4.7M_{\odot}/\text{MSTO}$ star⁸. This ratio is in excellent agreement with values derived using stellar population models for populations with $[\text{Fe}/\text{H}] \leq -1.5$; these models have values of $\sim 4M_{\odot}/\text{MSTO}$ star.

As is clear from Figs. 3 and 10, a significant part of the deviations from a smooth stellar halo is driven by the Sagittarius and Low-Latitude streams, and by the Virgo overdensity. We therefore run the whole minimization twice, once allowing all $b > 30^{\circ}$ data to define the fit, and a second time masking out most of the Sagittarius and Low-Latitude streams, and the Virgo overdensity, by masking regions with $b < 35^{\circ}$ and $0 < X < 30$, where X is the abscissa of the equal-area projection: $X = 63.63961\sqrt{2(1-\sin b)}$. This masking is done to constrain the importance of these larger structures in driving the model parameters and residual fraction.

4. RESULTS

In this section, we present the fitting results for a large set of smooth, symmetric stellar halos. In §4.1 we present the results from oblate stellar halos (i.e., the two longest axes have equal lengths). In §4.2, we discuss the fitting results for triaxial stellar halos (where all three axes can have different lengths), comparing this general case to the case of an oblate halo.

⁸Koch et al. (2004) find a deficit of low-mass stars in the central parts of Pal 5, suggesting that this ratio may be a lower limit.

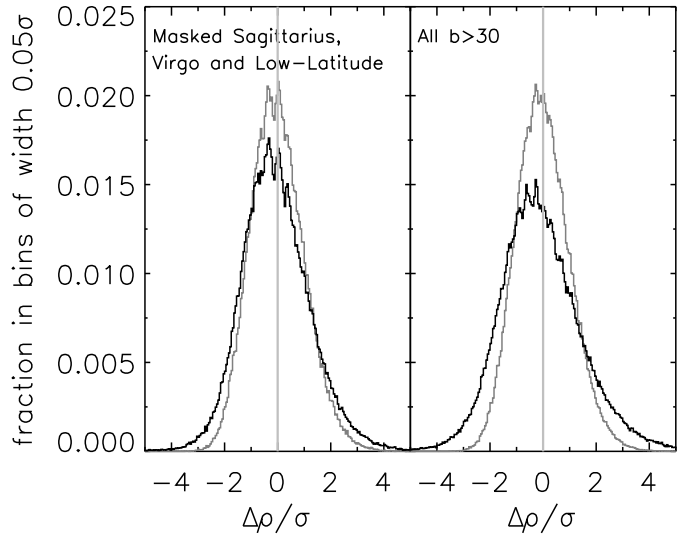


FIG. 5.— The distribution of differences between the observed star counts per $0.5^{\circ} \times 0.5^{\circ}$ pixel and that predicted by the best-fitting smooth model, divided by the σ predicted by Poisson uncertainties (black lines). The gray line shows the expected distribution from Poisson fluctuations around the smooth model. The left panel shows the distributions for the case in which sky areas of the Sagittarius, Virgo and Low-Latitude overdensities have been excised before this analysis; the right panel shows the results for all $b > 30^{\circ}$ data. Note that $\sim 1/2$ of the excess variance is in the ‘peak’ of the histogram (with $|\Delta\rho| < 3\sigma$), and the rest of the excess variance reflects a number of pixels with $|\Delta\rho| > 3\sigma$ (predominantly towards overdensities, rather than towards underdensities).

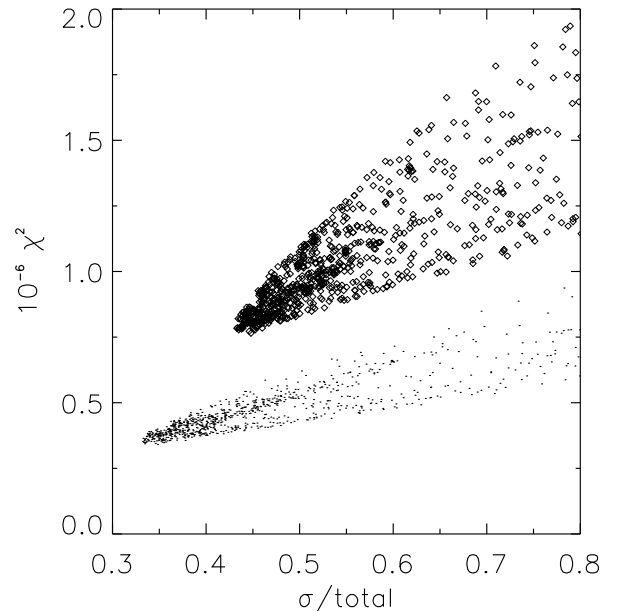


FIG. 6.— A comparison between σ/total and χ^2 for a large number of *oblate* halo models. Each point represents a different oblate halo model: open diamonds show the residuals when no clipping is applied (260456 degrees of freedom), points show the result when areas with contributions Sgr/Low-Latitude stream/Virgo are excised before carrying out the analysis (154336 degrees of freedom).

4.1. The ‘best fit’ smooth oblate halo model

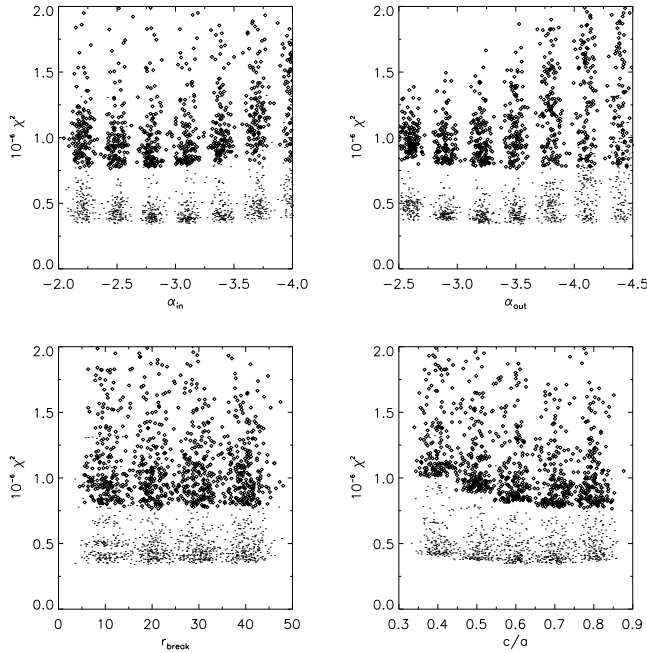


FIG. 7.— The χ^2 values of a large number of *oblate* halo models. The figure is formatted identically to Fig. 4.

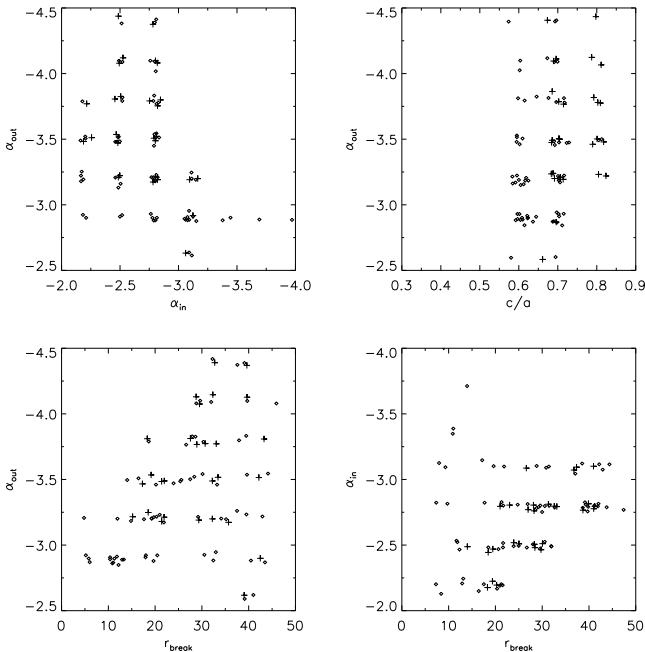


FIG. 8.— Covariance between different model parameters, for the ‘best’ *oblate* fits (diamonds show models with $\sigma/\text{total} < 0.45$, whereas crosses show models with $\chi^2 < 8 \times 10^5$) for which all data with $b > 30^\circ$ were fit. Small random offsets are applied to the discrete values of α_{in} , α_{out} , r_{break} and c/a to aid visibility.

In Fig. 4, we show how the residual fraction depends on the halo parameters for a survey of parameter space for oblate halos. It is immediately clear that these smooth models are a *very poor* representation of the structure of the stellar halo, with values of $\sigma/\text{total} \gtrsim 0.4$ for the best-fitting models for the case

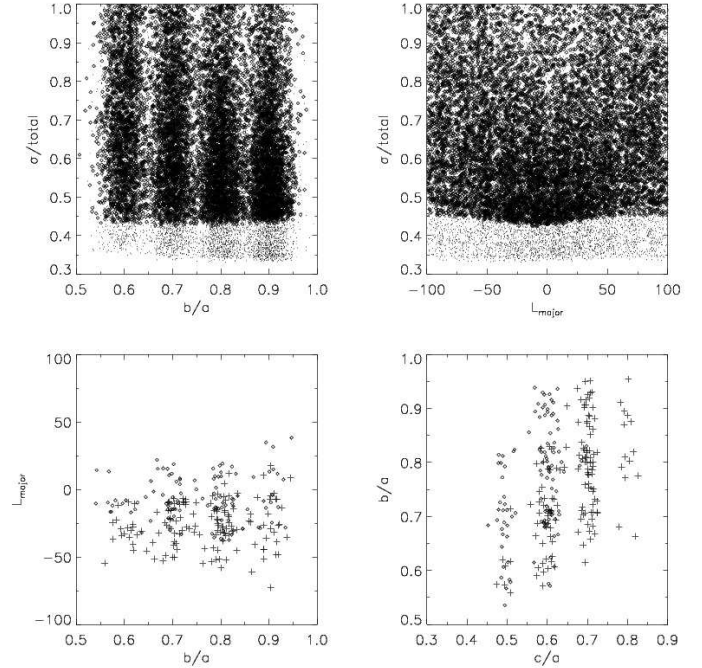


FIG. 9.— Data fitting results for the triaxial model halos, analogous to Fig. 4. In this figure, we show only the behavior of the ‘extra’ parameters required for a triaxial fit, as the behavior of α_{in} , α_{out} , r_{break} and c/a is similar to the oblate case shown in Fig. 4. Again, diamonds show the results for all data with $b > 30^\circ$, and the points for the case where Sagittarius, the Low-Latitude stream and the Virgo Overdensity were masked out. The top two panels show how RMS depends on b/a (where $b/a = 1$ is the oblate case and is not shown), and L_{major} , the angle between the long axis of and the GC-Sun line. In the bottom two panels, we show covariance between L_{major} and b/a , and b/a and c/a for model fits with $\sigma/\text{total} < 0.44$ (diamonds) and $\chi^2 < 7.8 \times 10^5$ (crosses) for which all data with $b > 30^\circ$ were been fit. Small random offsets are applied to the discrete values of b/a , L_{major} and b/a to aid visibility. Including triaxiality does not significantly improve the quality of fit; when triaxiality is included then values of L_{major} between -40 and 0 are favored, reflecting an attempt by the triaxial smooth halo model to fit out contributions from the Sagittarius tidal stream.

where all $b > 30^\circ$ data are fit, and $\sigma/\text{total} \gtrsim 0.33$ for the case where Sagittarius, Virgo and the Low-Latitude overdensities are clipped. Prolate models were attempted, and were all considerably poorer fits than the oblate case shown here (i.e., the trend towards poorer fits in Fig. 4 with increasing c/a continues for $c/a > 1$).

In Fig. 5, we show with the black lines the distribution of the differences between observed and smooth model distributions in $0.5^\circ \times 0.5^\circ$ bins for both the case where Sagittarius, Virgo and Low-Latitude structures were masked out (left panel) and for all $b > 30^\circ$ data (right panel). In grey, we show the distribution expected for Poisson noise around the smooth model alone. The difference between the observed histograms and the Poisson expectation is the signal which we observe ($\sigma/\text{total} \sim 0.33, 0.43$ for the clipped and unclipped datasets, respectively)⁹.

From inspection of Fig. 4, it is clear that a variety of different combinations of parameters are able to provide similar val-

⁹Note that the appearance of Fig. 5 depends on the adopted binning, through the contribution of Poisson uncertainties to the histogram of $\Delta\rho/\sigma$. The value of σ/total is both in principle and in practice independent of binning scale. Larger angular bins reduce the contribution of Poisson noise significantly, making the distribution of $\Delta\rho/\sigma$ significantly broader, while the value of σ/total is unchanged.

ues of σ/total . The oblateness of the halo is best-constrained, with values of $c/a \sim 0.6$ preferred¹⁰. This determination of halo oblateness is in excellent agreement with that of previous work (e.g., Chiba & Beers 2000; Chen et al. 2001; Larsen & Humphreys 2003; Lemon et al. 2004; Newberg & Yanny 2005; Jurić et al. 2007; Xu et al. 2006). Other parameters are less well-constrained: various combinations of α_{in} , α_{out} and r_{break} are capable of fitting the halo equally well. Best fit stellar halo masses (over a radius range of 1–40 kpc) come out at $\sim 3.7 \pm 1.2 \times 10^8 M_{\odot}$ for the models with $\sigma/\text{total} < 0.45$, with considerable uncertainty from the mass-to-number ratio.

In Figs. 6 and 7 we show the relationship between χ^2 and σ/total , and show the run of χ^2 as a function of the smooth halo model parameters. The minimum χ^2 is 7.65×10^5 with 260456 degrees of freedom for the case where all $b > 30^\circ$ data are fit, and 3.41×10^5 with 154336 degrees of freedom for the case where Sagittarius, the low-latitude stream and Virgo are excised from the fit; in both cases, the probability of the data being drawn from the model are zero (to within floating point precision). One can see that σ/total and χ^2 minimizations yield similar, but not identical results. The principal difference between σ/total and χ^2 minimization is that models with somewhat higher $c/a \sim 0.7$ are preferred. This is because of the $1/\sigma^2$ weighting of χ^2 , that gives higher weight to better-populated pixels (in our case, the pixels at larger radii; this tends to give Sagittarius high weight in driving the fit). Such a tendency towards higher c/a with at distances $\gtrsim 20$ kpc has been claimed before (Chiba & Beers 2000); we do not comment further on this possible trend here. Nonetheless, the key message of these plots is that minimization using χ^2 and subsequent estimation of σ/total yields similar results, but with slightly larger values of σ/total than our method, which chooses explicitly to minimize the metric of interest in order to put a lower limit on its value.

The covariance of the different fitting parameters of the oblate case is illustrated in Fig. 8. Models yielding $\sigma/\text{total} < 0.45$ are shown as diamonds, and $\chi^2 < 8 \times 10^5$ as crosses, where all data with $b > 30^\circ$ are used. It is clear that the degeneracies in α_{in} , α_{out} and r_{break} indicate that there are a number of different ways to construct reasonable halo models (see Robin, Reylé, & Crézé 2000 for similar results), with the general features of a power law $\alpha_{\text{out}} \sim -3$ in the outer parts and a similar or shallower power law in the very inner parts of the halo at Galactocentric radii $r_{\text{GC}} \lesssim 20$ kpc¹¹. It is important to note that the constraints on the ‘best fit’ halo model are very weak, owing to the significant degree of halo substructure.

4.2. Triaxial models

The results for triaxial models are shown in Fig. 9. We do not show the results for the power-law parameters α_{in} , α_{out} and r_{break} , nor the run of σ/total vs. c/a , as the results for these parameters is very similar to the oblate halo case. We focus instead on the results for the ‘new’ parameters b/a and L_{major} (the

angle between the long axis and the line between the Galactic Center [GC] and Sun).

The best triaxial fit is only very marginally better than the best oblate fit, with $\sigma/\text{total} = 0.42$; in particular, the best triaxial fit is still a very poor fit to the stellar halo of the Milky Way as judged by either σ/total or χ^2 . Inspection of Fig. 9 shows that the best models are only mildly triaxial with $b/a \gtrsim 0.8$, and with $L_{\text{major}} \sim -20$ (roughly lining up with the Sagittarius stream). In the bottom panels we show the covariance of the parameters of all models with $\sigma/\text{total} < 0.44$ (diamonds) or $\chi^2 < 7.8 \times 10^5$ (crosses). There is little obvious covariance between the ‘triaxiality’ parameters, or between the power law parameters and the triaxiality parameters. This stresses the difficulty in fitting a unique model to the halo; owing to the significant degree of halo substructure, there are many ways to fit the halo by balancing problems in one part of the halo against a better fit elsewhere.

4.3. A highly structured stellar halo

The key point of this paper is that a smooth and symmetric (either oblate/prolate or triaxial) model is a poor representation of the structure of the stellar halo of our Milky Way. The σ/total of the $b > 30^\circ$ data around the model is $> 42\%$; even if the largest substructures are clipped, the values of σ/total are $> 33\%$ (i.e., the largest substructures contain $\sim 40\%$ of the total variance).

One can obtain a visual impression of how poorly fit the stellar halo is by a smooth model by examining Fig. 10, which shows the mean stellar density residuals from the *best fit* oblate model. The residuals are smoothed by a $42'$ Gaussian kernel to suppress Poisson noise. One can see that the residuals are highly structured on a variety of spatial scales. Particularly prominent are contributions from the well-known Sagittarius tidal stream (dominating all residuals for $20.5 \leq r < 22.5$), the Low-Latitude stream (Galactic anticenter direction and $b < 35^\circ$), and the Virgo overdensity (particularly prominent in the $19.5 \leq r < 20$ slice as the diffuse overdensity centered at $(l, b) \sim (280, 70)$: see Jurić et al. 2007 and Newberg et al. 2007).

¹⁰The halo oblateness is affected by the assumed value of M_r . Variations of M_r of ± 0.5 mag lead to changes in oblateness of ∓ 0.1 . Furthermore, if the stellar halo has a binary fraction different from that of the globular clusters used to calibrate the absolute magnitude and scatter of turn-off stars, the values for absolute magnitude and scatter would be affected at the $\lesssim 0.3$ mag level, leading to modest changes in recovered oblateness (Larsen & Humphreys 2003).

¹¹It is interesting in this context that there have been claims of a break in the power law of the stellar halo at $r_{\text{GC}} \sim 20$ kpc from counts of RR Lyrae stars (see Preston et al. 1991, although other analyses see no evidence for a break, e.g., Chiba & Beers 2000).

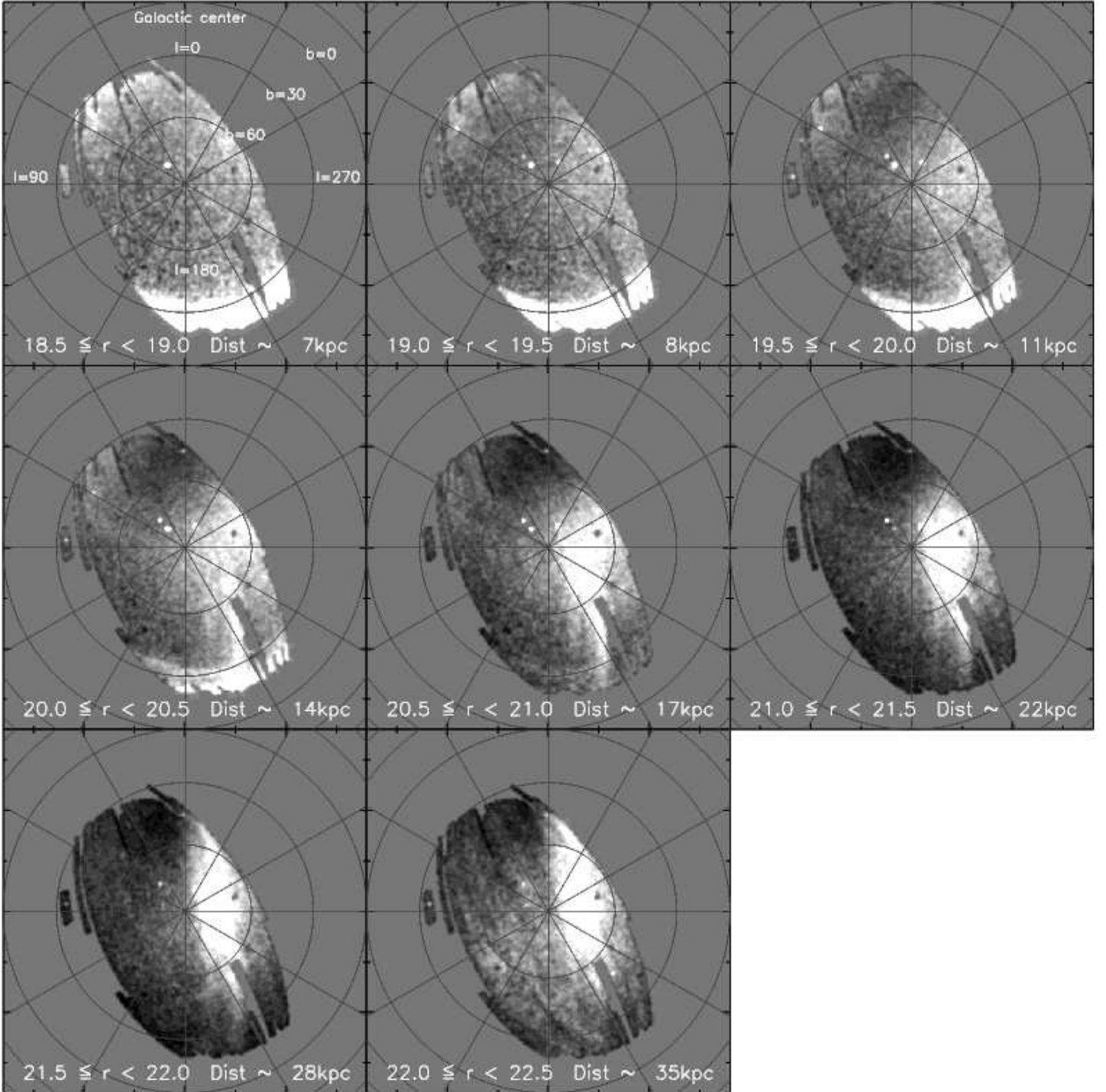


FIG. 10.— Residuals of the mean stellar density (data–model) from the best *oblate* model $(\alpha_{\text{in}}, \alpha_{\text{out}}, r_{\text{break}}, c/a) = (-2.2, -3.5, 20 \text{ kpc}, 0.7)$. The panels show 8 different distance slices, and have been smoothed using a $\sigma = 42'$ Gaussian. The gray scale saturates at $\pm 60\%$ deviation from the model density, and white represents an observed excess over the smooth model prediction.

There are a number of other less obvious structures. In the last three magnitude bins, one can discern the ‘Orphan Stream’ (Belokurov et al. 2006b; Grillmair 2006a), starting at $(l, b) \sim (250, 50)$ and stretching to $(l, b) \sim (170, 40)$ before disappearing into the noise (there is a clear distance gradient, such that as l decreases the distance increases). Visible also is a recently-identified structure of stars stretching from $(l, b) \sim (180, 75)$ towards $(l, b) \sim (45, 45)$. This structure, called the Hercules-Aquila Overdensity by Belokurov et al. (2007), extends south of the Galactic plane (as shown in that paper) and is at a distance of ~ 16 kpc from the Sun. The Hercules-Aquila Overdensity is reflected as a distinct overdensity in color–magnitude space, shown in the lower middle panel of Fig. 1. This CMD, obtained by subtracting a background field at $(l, b) \sim (15, 45)$ from an overdensity field at $(l, b) \sim (44, 40)$, shows a somewhat broadened MSTO with turn-off color $g-r \sim 0.3$ (i.e., a similar color to the rest of the stellar halo). Fig. 10 illustrates that this very diffuse overdensity lies in a ‘busy’ area of the halo, making its extent difficult to reliably estimate. There are other potential structures visible, in particular in the most distant $22 \leq r < 22.5$ bin. Some of the structure has low-level striping following the great circles along which the SDSS scans¹², indicating that the structure is an artifact of uneven data quality in different stripes. Other structures have geometry more suggestive of genuine substructure; we choose to not speculate on the reality (or ‘distinctness’) of these structures at this stage owing to the decreasing data quality at these faint limits.

4.4. Structure as a function of distance

The visual impression given by Fig. 10 suggests an increasing amount of deviation from a smooth halo at larger heliocentric distances. We quantify this in Fig. 11, where we show the σ/total as a function of apparent magnitude for all stars with $b > 30^\circ$ (diamonds). While it is clear that the exact values of σ/total will depend somewhat on which smooth model happens to fit best, the value of σ/total doubles from distances of ~ 5 kpc to ~ 30 kpc. From comparison with the case when Sagittarius, the Low-Latitude stream and the Virgo overdensity are removed before calculation of the RMS, one can see that much of this increase in RMS is driven by the few large structures; i.e., much of the RMS is contained in a few very well-defined structures at large radii.

5. COMPARISON WITH EXPECTATIONS FROM A Λ CDM UNIVERSE

In this paper, we have attempted to fit smooth models to the stellar halo of the Milky Way. Models containing $3.7 \pm 1.2 \times 10^8 M_\odot$ in the radial range 1–40 kpc with power-law density distributions $\rho \sim r^{-3}$ were favored, *although all smooth models were a very poor fit to the data*. We have found that the stellar halo of the Milky Way halo is richly substructured, with $\sigma/\text{total} \gtrsim 0.4$. The fractional amount of substructure appears to increase with radius; this increase is driven primarily by a few large structures.

To put our results into a cosmological context, we compare the observations to predictions for stellar halo structure from appropriate models. Bullock, Kratsov, & Weinberg (2001) and

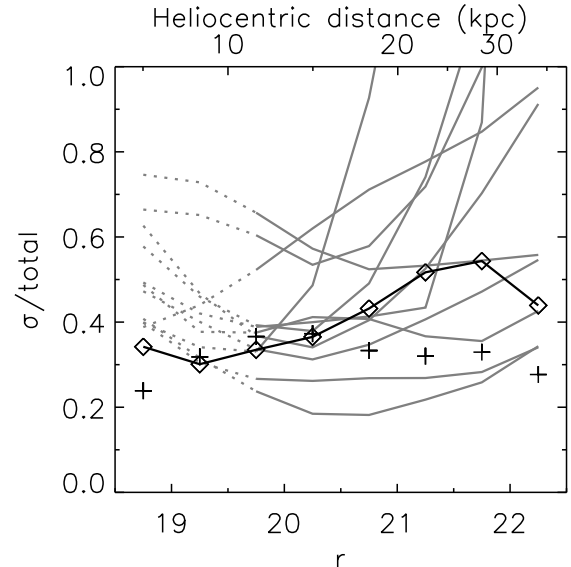


FIG. 11.— The substructure in the Milky Way stellar halo, compared to predictions from cosmological models. The σ/total as a function of apparent magnitude (distance assuming $M_r \sim 4.5$) for the ‘best fit’ oblate model. Diamonds denote the SDSS results for all $b > 30^\circ$ data; crosses denote analogous results when the bulk of the Sagittarius and Low-Latitude tidal streams, and the Virgo overdensity, have been excised from consideration. The ensemble of solid gray lines show the predictions for σ/total from 11 models of stellar halo growth in a cosmological context from Bullock & Johnston (2005); dotted lines are used at small radii where the simulations are likely to be less robust. In these simulations the entire halo arises, by model construction, from the disruption of satellite galaxies.

Bullock & Johnston (2005) studied the structure of stellar halos created *exclusively* through the merging and disruption of reasonably realistic satellite galaxies.¹³ These studies found that the debris from disrupted satellite galaxies produced stellar halos with: *i*) roughly power-law profiles with $\alpha \sim -3$ over 10–30 kpc from the galactic center (e.g., Fig. 9 of Bullock & Johnston 2005, see also Diemand, Madau, & Moore 2005, Moore et al. 2006), *ii*) total stellar halo masses from $\sim 10^9 M_\odot$ (integrated over all radii), and *iii*) richly substructured halos with increasingly evident substructure at larger distances (e.g., Figs. 13 and 14 of Bullock & Johnston 2005).

¹²This striping has a modest effect on our measurement of σ/total , as illustrated in Fig. 11. There are two main effects, working in counteracting directions: on one hand, the striping will introduce a small amount of excess variance, on the other hand, galaxies misclassified as stars are smoothly distributed across the sky, reducing the variance. We chose to include the $22 \leq r < 22.5$ bin in the analysis, noting that its exclusion does not affect our results or conclusions.

¹³Abadi, Navarro, & Steinmetz (2006) analyzed the properties of the stellar halo of a disk galaxy formed in a self-consistent cosmological simulation. Such a self-consistent simulation does not require that stellar halos be built up solely through accretion; yet, the final halos produced were very similar to those of Bullock, Kratsov, & Weinberg (2001) and Bullock & Johnston (2005).

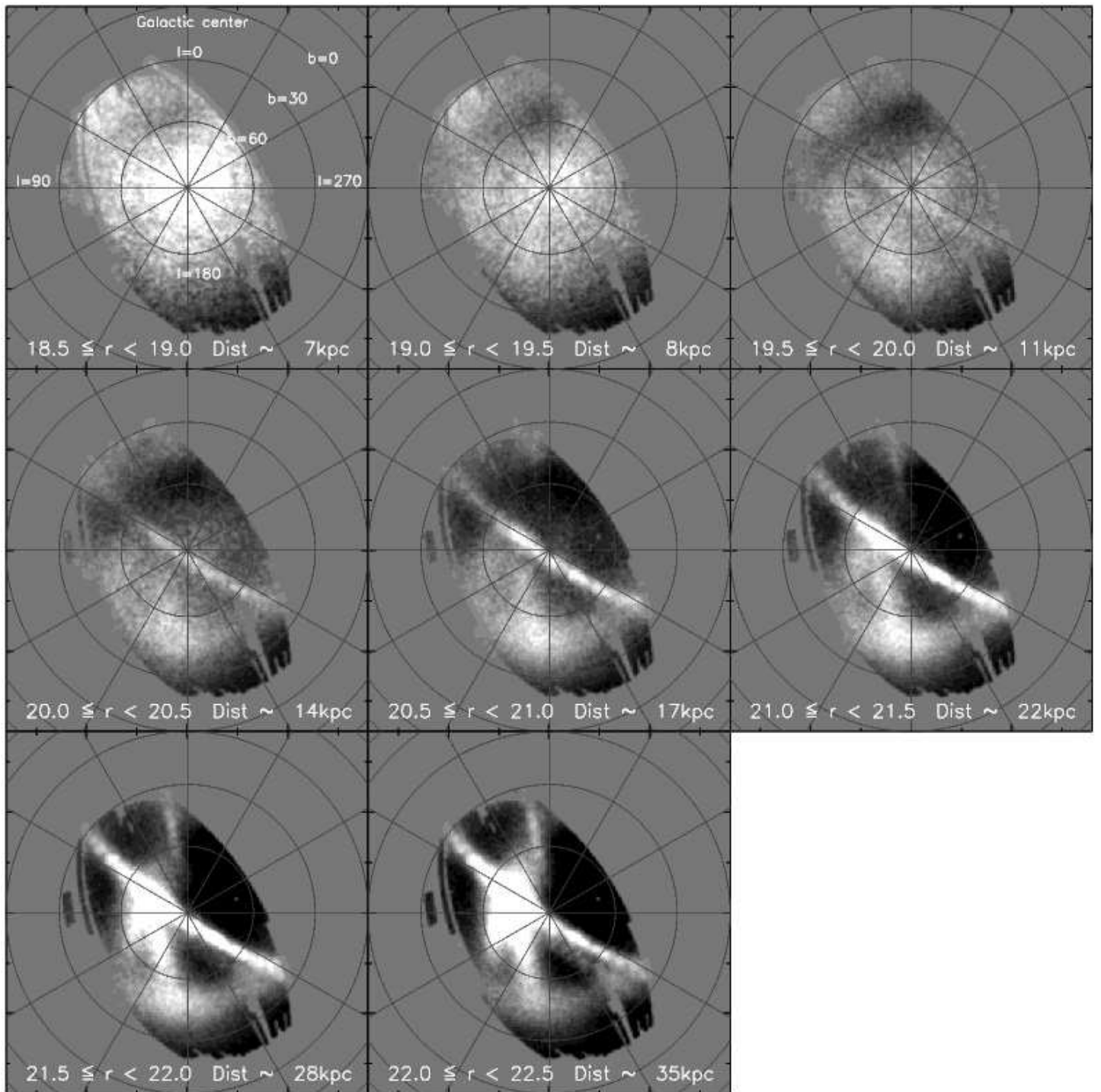


FIG. 12.— Residuals (simulation–smooth model) smoothed using a $\sigma = 42'$ Gaussian from the best *oblate* model for Model 2 from Bullock & Johnston (2005) in 8 different distance slices. The gray scale saturates at $\pm 60\%$ from the smooth model density.

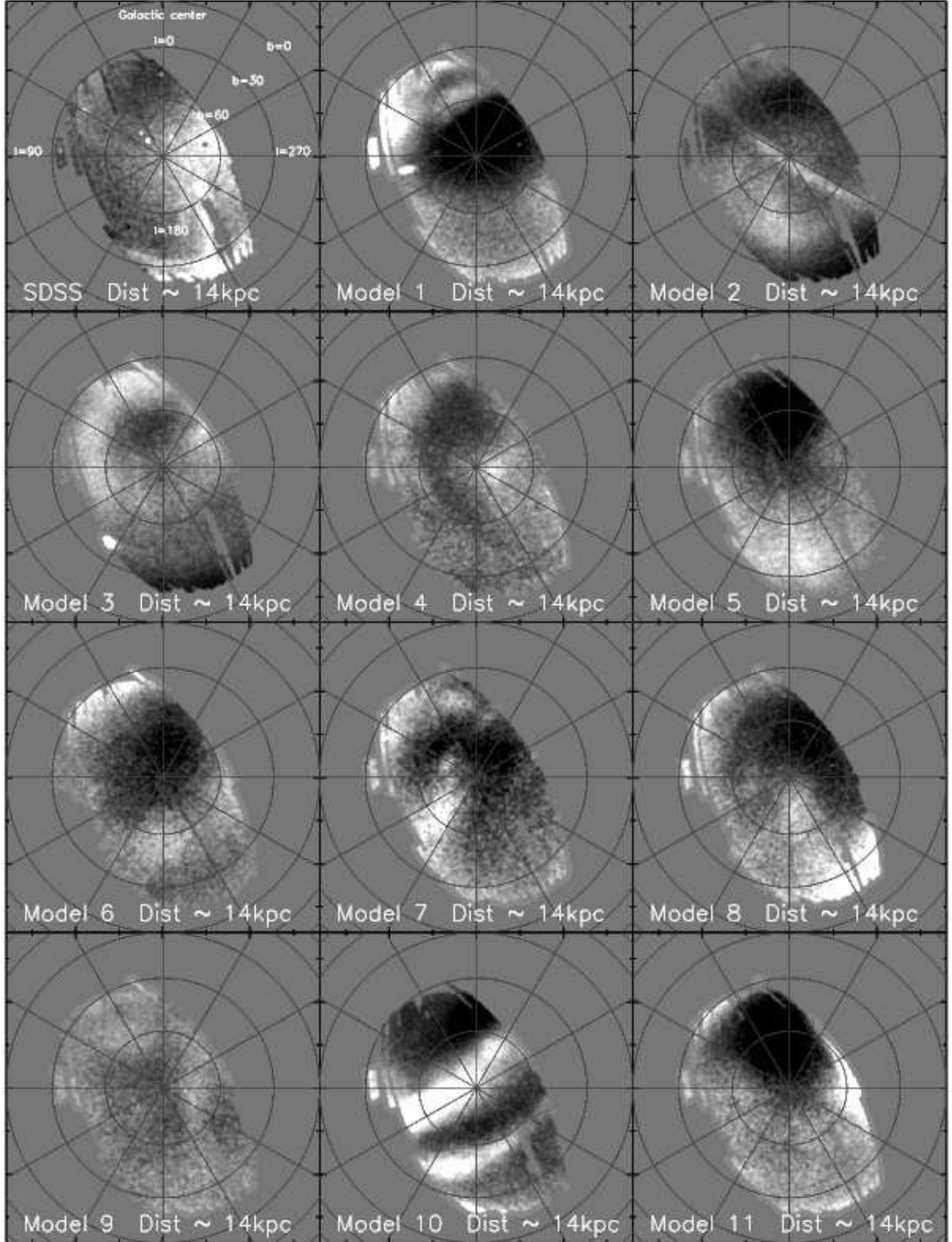


FIG. 13.— Residuals (SDSS or simulations minus the smooth model) smoothed using a $\sigma = 42'$ Gaussian from the best *oblate* model fits for the SDSS data (top left panel) and for the 11 simulations from Bullock & Johnston (2005). We show only the $20 \leq r < 20.5$ slice, corresponding to heliocentric distances ~ 14 kpc. The gray scale saturates at $\pm 60\%$ from the smooth model density.

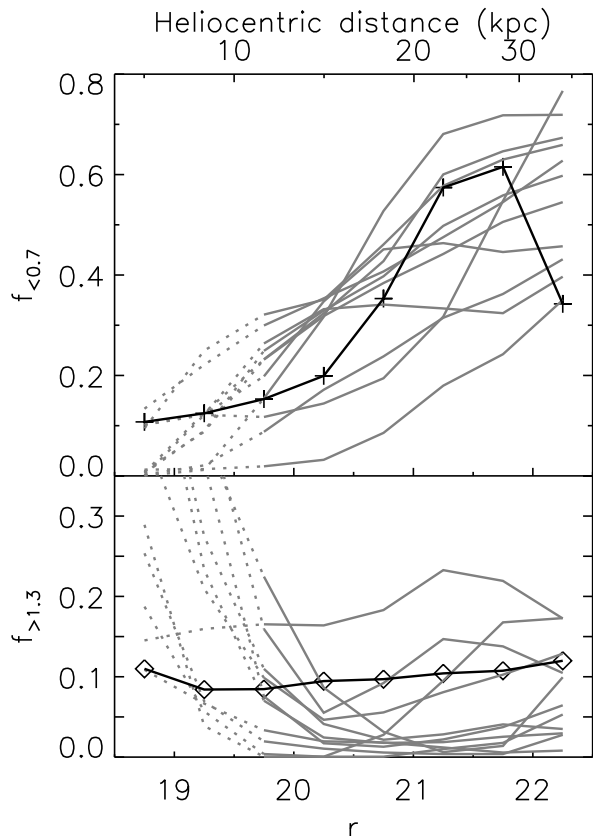


FIG. 14.— The fraction of the SDSS footprint in areas with $< 70\%$ of the smooth model density (upper panel) and $> 130\%$ of the smooth model density (lower panel) in both the observations (black line with symbols) and the 11 simulations from Bullock & Johnston (2005, gray lines). Dotted lines denote where the simulations are argued to be less robust.

5.1. A quantitative comparison with simulated stellar halos

We quantify the last statement through comparison of the SDSS data for the stellar halo with 11 simulated stellar halos from Bullock & Johnston (2005)¹⁴. These 11 simulated halos were generated at random using semi-analytic merger trees appropriate for a Λ CDM cosmology for a Milky-Way mass dark matter halo. Maps of MSTO stars (analogous to our SDSS data) were constructed from the simulated N -body stellar halos, accounting for all important observational effects, as follows. The number of MSTO stars per particle was estimated using a ratio of 1 main sequence turn off star for every $8 L_{\odot}$, as calibrated empirically using Palomar 5. MSTO stars were distributed in space by smoothing over the 64 nearest N -body particle neighbors, using a Epanechnikov kernel of the form $(1-r^2)$. Each star was assigned a simulated Galactic latitude, longitude, and heliocentric distance assuming that the Sun is 8 kpc from the Galactic center. The heliocentric distance is used to generate

¹⁴The number of particles in the stellar halo of the Abadi, Navarro, & Steinmetz (2006) model galaxy was unfortunately too small to permit a proper comparison with the SDSS data.

r -band apparent magnitudes for the MSTO stars assuming an absolute magnitude $M_r = 4.5$ and scatter $\sigma_{M_r} = 0.9$ (following §3). The models were then placed in a Lambert equal-area projection, and the survey limits of the SDSS DR5 data analyzed in this paper applied to the simulated maps. These simulations were analyzed in the same way as the SDSS data, by fitting the same grid of oblate models. The results are shown in Fig. 11, and Figs. 12 and 13.

Fig. 11 shows the main result of this analysis: all simulations predict a great deal of halo substructure, with values of $\sigma/\text{total} \gtrsim 0.2$. The typical smooth halo fitting parameters (where we quote the average and scatter derived from the fits to the 11 simulated stellar halos) are similar to that of the Milky Way’s halo with $\alpha_{\text{out}} \sim -3.4 \pm 0.6$, $M_{1 < r/\text{kpc} < 40} \sim 2.8 \pm 1.5 \times 10^8 M_{\odot}$, and $c/a \sim 0.65 \pm 0.25$; values of α_{in} within $r_{\text{break}} \sim 25$ kpc tend to be higher than that observed for the Milky Way at -1.3 ± 0.7 . At small Galactocentric radii $\lesssim 15$ kpc, the simulations are expected to be much too structured (owing to the lack of a live Galactic potential, see §4.2 of Bullock & Johnston 2005); accordingly, we show results for heliocentric distances $\lesssim 10$ kpc as dotted lines, and place little weight on the relatively high values of α_{in} recovered by the best-fitting models. At larger radii, where the simulation results are expected to be more robust, there are model halos with both less structure and more structure than the Milky Way’s stellar halo. We illustrate this result in Figs. 12 and 13. Fig. 12 shows the residuals (simulation–best fit smooth halo) for a model with very similar σ/total to the Milky Way on the same grey scale used for Fig. 10 in eight different apparent magnitude slices. Fig. 13 illustrates the diversity of simulated halos, showing the $20 \leq r < 20.5$ apparent magnitude slice (corresponding to heliocentric distances ~ 14 kpc) for the SDSS and the 11 Λ CDM realizations of Milky Way mass stellar halos. A number of the general characteristics of the simulations match the characteristics of the SDSS data: the angular extent of ‘features’ in the nearest bins is typically very large, whereas the angular width of streams in the distant bins tends to be smaller. In the distant bins, the halo substructure is a combination of well-confined, relatively young streams and diffuse sheets of stars from both older disruption events and young events on almost radial orbits (K. Johnston et al., in preparation), with large-scale overdensities and underdensities being seen.

In Fig. 14, we explore the fraction of area in under- and overdensities in both the observations (black lines and symbols) and the 11 Λ CDM realizations of Milky Way Mass stellar halos (gray lines). We quantify this by comparing the fraction of area for each apparent magnitude slice with densities 30% or more below the smooth model at that radius ($f_{<0.7}$, shown in the upper panel), and the fraction of the area in each slice with densities 30% or more above the smooth model at that radius ($f_{>1.3}$, in the lower panel). This comparison is sub-optimal in the sense that both the model and data have a non-zero contribution from Poisson noise (the immunity to Poisson noise was one of the key advantages of the σ/total estimator), although we have reduced the Poisson noise by rebinning the data and models in 4×4 pixel bins; with this rebinning, the variance from counting uncertainties is 16 times smaller than the intrinsic variance. One can see the expected result that much of the sky area is covered in underdensities, with a smaller fraction of the sky in overdensities. Again, the models at Galactocentric radii $\gtrsim 15$ kpc (where they are reliable) reproduce the general behavior of the observed stellar halo rather well. Interestingly,

the fraction of sky area in overdensities tends to be somewhat lower in the models than in the observations (i.e., there may be room for the models to predict *more* substructure).

This comparison shows that the overall level of the substructure seen in the Milky Way’s stellar halo falls into the middle of the range of predictions from simulations — simulations in which the stellar halo arises exclusively from the merging and disruption of satellite galaxies. Furthermore, the character of the structures in the simulated stellar halos is very similar to those observed in the Milky Way¹⁵. The models clearly have some shortcomings; in particular, the use of a slowly-growing rigid potential for the central disk galaxy in the Bullock & Johnston (2005) simulations leads to excess structure in the central parts. Furthermore, it is possible that the real stellar halo has a ‘smooth’ component formed either *in situ* in the potential well of the galaxy or accreted so early that no spatial structure remains. Our analysis shows that there is no need for such a smooth component to explain the data, and suggests that a smooth component does not dominate the halo at radii $5 < r_{\text{GC}}/\text{kpc} < 45$. Yet, we have not tested quantitatively how large a smooth component could lie in this radial range and still lead to the observed RMS: such an exercise will be the object of a future work.

5.2. Limitations of this comparison

While there are steps which can and will be taken with this dataset to sharpen the comparison with the simulations (e.g., a quantitative comparison of the morphology and spatial scale of substructure, and the investigation of substructure metallicities), it is nonetheless clear that ‘small number statistics’ is a key limitation of this work. The SDSS DR5 contiguously covers only 1/5 of the sky, encompassing some 5–10% of all halo stars, with Galactocentric radii between 5 and 45 kpc (as estimated by comparison of the smooth halo stellar masses with the actual mass contained in the maps). Larger and deeper multi-color imaging surveys will be required to expand the coverage of the Milky Way’s stellar halo, probing to larger halo radii where models predict that halo substructure should be easier to discern (see, e.g., the prominent substructures discovered by Sesar et al. 2007 using RR Lyrae stars in the multiply-imaged ‘Stripe 82’ of the SDSS). Yet, there is significant halo-to-halo scatter in the simulated stellar halos; thus, matching the properties of a *single* stellar halo will always be a relatively easy task. More powerful constraints will come from studies of the stellar halos of statistical samples of galaxies using high-resolution ground-based or HST data (see encouraging progress from e.g., Ferguson et al. 2002 and de Jong et al. 2007).

6. CONCLUSIONS

In this paper, we have quantified the degree of (sub-)structure in the Milky Way’s stellar halo. We have used a sample of stellar halo main sequence turn-off stars, isolated using a color cut of $0.2 < g-r < 0.4$, and fit oblate and triaxial broken power-law models of the density distribution to the data.

We find that the ‘best’ fit oblateness of the stellar halo is $0.5 < c/a < 0.8$ over the Galactocentric radial range 5 to 40 kpc. Other halo parameters are significantly less well-constrained; many different combinations of parameters (including mild triaxiality) can provide comparably good fits. A single power

law $\rho \propto r^\alpha$ with $\alpha = -3$ provides an acceptable fit. Values of $-2 > \alpha > -4$ are also reasonable fits, as are halo profiles with somewhat shallower slopes at $r \lesssim 20$ kpc and steeper slopes outside that range. The halo stellar mass of such models between Galactocentric radii of 1 and 40 kpc is $3.7 \pm 1.2 \times 10^8 M_\odot$, with considerable uncertainty from the conversion of the number of $0.2 < g-r < 0.4$ turn-off stars to mass.

Importantly, we find that *all* smooth models are very poor fits to the spatial distribution of stellar halo stars. Deviations from smooth parameterized distributions, quantified using the RMS of the data around the model fit in $0.5^\circ \times 0.5^\circ$ bins (>100 pc scales at the distances of interest) give $\sigma/\text{total} \gtrsim 0.4$, after subtracting the (known) contribution of Poisson counting uncertainties. Furthermore, the halo seems significantly more structured at larger radii than in the inner ~ 10 kpc; a few individual structures dominate this increase in σ/total at larger radii.

Qualitatively, these results show that the stellar ‘substructure’ found in the Milky Way’s halo is not at all a small perturbation on top of a smooth halo. Remarkably, this same conclusion holds when excising the most prominent known substructures from the analysis, such as the Sagittarius stream, and then considering the remaining area of the sky.

We compared these observational results with models of stellar halo growth in a cosmological context taken from Bullock & Johnston (2005). In these models, the stellar halo arises exclusively from the disruption of and mergers with satellite galaxies. The models were analyzed in the same way as the SDSS data. Their models predict $\alpha \sim -3$ in the radial range 10–30 kpc, halo masses $\sim 10^9 M_\odot$ integrated over all radii (or masses $\sim 3 \times 10^8 M_\odot$ in the radial range 1–40 kpc), and richly-structured stellar halos with $\sigma/\text{total} \gtrsim 0.2$. At radii where the model predictions are most robust, the models show a range of degrees of substructure, from substantially less than that observed for the Milky Way to substantially more. Furthermore, the character of the substructure appears very similar to that showed by the Milky Way’s stellar halo. While it is clear that the models are not perfect, this comparison lends considerable quantitative weight to the idea that a dominant fraction of the stellar halo of the Milky Way is composed of the accumulated debris from the disruption of dwarf galaxies.

We thank the anonymous referee for their excellent suggestions, and for encouraging exploration of the fraction of material in under- and overdensities. We thank Jun-Hwan Choi and Martin Weinberg for useful discussions. E. F. B. thanks the Deutsche Forschungsgemeinschaft for their support through the Emmy Noether Program. D. B. Z. was supported by a PPARC-funded rolling grant position. V. B. was supported by a PPARC Fellowship. T. C. B. acknowledges partial support for this work from grant PHY 02-16783, Physics Frontier Center/Joint Institute for Nuclear Astrophysics (JINA), awarded by the US National Science Foundation.

Funding for the SDSS and SDSS-II has been provided by the Alfred P. Sloan Foundation, the Participating Institutions, the National Science Foundation, the U.S. Department of Energy, the National Aeronautics and Space Administration, the Japanese Monbukagakusho, the Max Planck Society, and the Higher Education Funding Council for England. The SDSS Web Site is <http://www.sdss.org/>.

The SDSS is managed by the Astrophysical Research Consortium for the Participating Institutions. The Participating Institutions are the American Museum of Natural History, As-

¹⁵Model 2 in particular matches the trend in RMS with Heliocentric distance and the fraction in over/underdensities to within $\lesssim 0.1$ for all bins with distance $\gtrsim 10$ kpc.

trophysical Institute Potsdam, University of Basel, Cambridge University, Case Western Reserve University, University of Chicago, Drexel University, Fermilab, the Institute for Advanced Study, the Japan Participation Group, Johns Hopkins University, the Joint Institute for Nuclear Astrophysics, the Kavli Institute for Particle Astrophysics and Cosmology, the Korean Scientist Group, the Chinese Academy of Sciences (LAMOST), Los Alamos National Laboratory, the Max-Planck-Institute for Astronomy (MPIA), the Max-Planck-Institute for Astrophysics (MPA), New Mexico State University, Ohio State University, University of Pittsburgh, University of Portsmouth, Princeton University, the United States Naval Observatory, and the University of Washington.

REFERENCES

- Abadi, M. G., Navarro, J. F., & Steinmetz, M. 2006, *MNRAS*, 365, 747
 Adelman-McCarthy, J. K., et al. 2007, submitted to *ApJS*
 Belokurov, V., et al. 2006a, *ApJ*, 642, L137
 Belokurov, V., et al. 2007, *ApJ*, 658, 337
 Belokurov, V., et al. 2007, *ApJ*, 657, L89
 Bullock, J. S., Kratsov, A. V., & Weinberg, D. H. 2001, *ApJ*, 548, 33
 Bullock, J. S., & Johnston, K. V. 2005, *ApJ*, 635, 931
 Chen, B., et al. 2001, *ApJ*, 553, 184
 Chiba, M., & Beers, T. C. 2000, *AJ*, 119, 2843
 de Jong, R. S., et al. 2007, to appear in the proceedings of IAU Symposium 241 (astro-ph/0702168)
 Diemand, J., Madau, P., & Moore, B. 2005, *MNRAS*, 364, 367
 Duffau, S., Zinn, R., Vivas, A. K., Carraro, G., Méndez, R., Winnick, R., & Gallart, C. 2006, *ApJ*, 636, L97
 Eggen, O. J., Lynden-Bell, D., & Sandage, A. R., 1962, *ApJ*, 136, 748
 Ferguson, A. M. N., Irwin, M. J., Ibata, R. A., Lewis, G. F., & Tanvir, N. R. 2002, *AJ*, 124, 1452
 Font, A. S., Johnston, K. V., Bullock, J. S., & Robertson, B. E. 2006, *ApJ*, 638, 585
 Fukugita, M., Ichikawa, T., Gunn, J. E., Doi, M., Shimasaku, K., & Schneider, D. P. 1996, *AJ*, 111, 1748
 Girardi, L., Grebel, E. K., Odenkirchen, M., & Chiosi, C. 2004, *A&A*, 422, 205
 Grillmair, C. J. 2006a, *ApJ*, 645, L37
 Grillmair, C. J. 2006b, *ApJ*, 651, L29
 Grillmair, C. J., & Dionatos, O. 2006, *ApJ*, 643, L17
 Grillmair, C. J., & Johnson, R. 2006, *ApJ*, 639, L17
 Gunn, J.E. et al. 1998, *AJ*, 116, 3040
 Gunn, J.E. et al. 2006, *AJ*, 131, 2332
 Harris, W. E. 1996, *AJ*, 112, 1487
 Helmi, A., & White, S. D. M. 1999, *MNRAS*, 307, 495
 Hogg, D.W., Finkbeiner, D.P., Schlegel, D.J., Gunn, J.E. 2001, *AJ*, 122, 2129
 Ibata, R. A., Gilmore, G., & Irwin, M. J. 1995, *MNRAS*, 277, 781
 Ibata, R. A., Irwin, M. J., Lewis, G. F., Ferguson, A. M. N., & Tanvir, N. 2003, *MNRAS*, 340, L21
 Ibata, R. A., Irwin, M. J., Lewis, G. F., Ferguson, A. M. N., & Tanvir, N. 2001, *Nature*, 412, 49
 Irwin, M., & Hatzidimitriou, D. 1995, *MNRAS*, 277, 1354
 Ivezić, Ž., et al. 2000, *AJ*, 120, 963
 Ivezić, Ž. et al. 2004, *AN*, 325, 583
 Johnston, K. V. 1998, *ApJ*, 495, 297
 Jurić M., et al. 2007, *ApJ*, submitted (astro-ph/0510520)
 Koch, A., Grebel, E. K., Odenkirchen, M., Martínez-Delgado, D., & Caldwell, J. A. R. 2004, *AJ*, 128, 2274
 Larsen, J. A., & Humphreys, R. M. 2003, *AJ*, 125, 1958
 Laird, J. B., Carney, B. W., Rupen, M. P., & Latham, D. W. 1988, *AJ*, 96, 1908
 Lemon, D. J., Wyse, R. F. G., Liske, J., Driver, S. P., & Horne, K. 2004, *MNRAS*, 347, 1043
 Lupton, R., Gunn, J., & Szalay, A. 1999, *AJ*, 118, 1406
 Majewski, S. R. 1993, *ARA&A*, 31, 575
 Majewski, S. R., Munn, J. A., & Hawley, S. L. 1996, *ApJ*, 457, L73
 Majewski, S. R., Skrutskie, M. F., Weinberg, M. D., & Ostheimer, J. C. 2003, *ApJ*, 599, 1082
 Martínez-Delgado, D., Alonso-García, J., Aparicio, A., & Gómez-Flechoso, M. A. 2001, *ApJ*, 549, L63
 Momany, Y., Zaggia, S., Gilmore, G., Piotto, G., Carraro, G., Bedin, L. R., & de Angeli, F. 2006, *A&A*, 451, 515
 Moore, B., Diemand, J., Madau, P., Zemp, M., & Stadel, J. 2006, *MNRAS*, 368, 563
 Newberg, H. J., et al. 2002, *ApJ*, 569, 245
 Newberg, H. J., & Yanny, B., *Journal of Physics: Conf. series*, Volume 47, Issue 1, pp. 195-204
 Newberg, H. J., & Yanny, B., Cole, N. 2007, in preparation
 Odenkirchen, M., Grebel, E. K., Dehnen, W., Rix, H.-W., & Cudworth, K. M. 2002, *AJ*, 124, 1497
 Odenkirchen, M., et al. 2003, *AJ*, 126, 2385
 Peñarrubia, J., et al. 2005, *ApJ*, 626, 128
 Pier, J.R., Munn, J.A., Hindsley, R.B., Hennessy, G.S., Kent, S.M., Lupton, R.H., Ivezić, Z. 2003, *AJ*, 125, 1559
 Preston, G. W., Shectman, S. A., & Beers, T. C. 1991, *ApJ*, 375, 121
 Robin, A. C., Reylé, C., & Crézé, M. 2000, *A&A*, 359, 103
 Schlegel, D., Finkbeiner, D., & Davis, M. 1998, *ApJ*, 500, 525
 Searle, L., & Zinn, R. 1978, *ApJ*, 225, 357
 Sesar, B., et al. 2007, submitted to *AJ* (arXiv:0704.0655)
 Shang, Z., et al. 1998, *ApJ*, 504, L23
 Smith, J. A., et al. 2002, *AJ*, 123, 2121
 Stoughton, C. et al. 2002, *AJ*, 123, 485
 Tucker, D., et al. 2006, *AN*, 327, 821
 Venn, K. A., Irwin, M., Shetrone, M. D., Tout, C. A., Hill, V., & Tolstoy, E. 2004, *AJ*, 128, 1177
 Xu, Y., Deng, L. C., & Hu, J. Y. 2006, *MNRAS*, 368, 1811
 Yanny B., et al 2000, *ApJ*, 540, 825
 Yanny B., et al 2000, *ApJ*, 588, 824
 York D.G., et al. 2000, *AJ*, 120, 1579